From microscale to boundary value problem: using a micromechanically-based model

Hao Xiong[a], François Nicot[a], Zhenyu Yin[b,c,*]

[a] *Université Grenoble Alpes, IRSTEA, Geomechanics Group, ETNA, Grenoble, France*
[b] *Department of Civil and Environmental Engineering, The Hong Kong Polytechnic University, Hung Hom, Kowloon, Hong Kong, China*
[c] *Research Institute of Civil Engineering and Mechanics (GeM), UMR CNRS 6183, Ecole Centrale de Nantes, France*

Abstract

A 3D multi-scale approach is presented to investigate the mechanical behavior of a macroscopic specimen consisting of a granular assembly, as a boundary value problem. The core of this approach is a multiscale coupling, wherein the finite element method is used to solve a boundary value problem and a micromechanically-based model is employed as constitutive relationship used at a representative volume element scale. This approach provides a convenient way to link the macroscopic observations with intrinsic microscopic mechanisms. The plane-strain triaxial loading condition is selected to simulate the occurrence of strain localization. A series of tests are performed, wherein distinct failure patterns are observed and analyzed. A system of shear band naturally appears in a homogeneous setting specimen. By defining the shear band area, microstructural mechanisms are separately investigated inside and outside the shear band. The normalized second order

*Corresponding author.
Email address: zhenyu.yin@gmail.com (Zhenyu Yin)

work introduced as an indicator of instability occurrence is analyzed not only on the macroscale but also on the microscale.

Keywords: Multiscale approach, Micromechanics, Second-order work, Mesoscopic scale, Granular materials, FEM, Strain localization, Shear band

1. Introduction

Granular materials contribute significantly to geotechnical engineering, generating considerable researches to observe, investigate and understand their complex behavior when subjected to loading paths. One of the phenomena observed refers to the instability occurrence, related to two kinds of failure modes: localized and diffuse [9, 30]. The strain localization including shear bands, compaction bands and dilation bands has a common characteristic: the existence of intensive deformation in narrow zones. This kind of failure with concentrated deformations is considered as a bifurcation problem.

When loading in a quasi-static regime, a material system can fail if the material cannot develop an internal stress able to balance the external loading. In these conditions, the excess external work will result in an increase in kinetic energy. Thus, the response of the material bifurcates from a quasi-static regime toward a dynamical regime [26, 29, 32]. This bifurcation, properly detected by the vanishing of the second-order work (see detailed definition in Chapter 3 of [41]), corresponds to a failure mode of the material system. The associated bifurcation at the material point level is conventionally triggered around the stress peak of a strain softening material or at the plastic threshold. The problem underlies a material instability phenomenon that originates in the small scale due to the micro-structural features of the granular material. As such, developing a micromechanically-based constitutive model of granular material is desired.

From microscale to BVPs (boundary value problems), the micromechanically-based model utilizes a multi-scale approach as a convenient process in bridging both micro-scale and macro-scale [27, 28]. Moreover, the multi-scale approach can also link a continuum-based method to a discontinuum-based method. Generally, the FEM (finite element method) is considered to solve the BVP on the macro-scale, while the DEM (discrete element method) [8, 35] is usually considered effective to capture and consider the behavior on the micro-structural scale. Both are leading trends of numerical simulation and sometimes can be beneficially coupled. For example, an FEM×DEM scheme is implemented to simulate the slope stability and strain localization problems [24, 25]. However, a continuum-based assumption (Taylor assumption [40]) is employed on the micro-scale, which may lead some limitations for a granular medium. [2] and [3] proposed a discrete-continuum method based on a numerical homogenization scheme to simulate the strain localization problem in granular materials. This approach utilizes a classical plastic model on the macro-scale involving two phenomenological parameters (friction angle and dilation angle), which are transferred from the micro-scale. [5, 6, 46–49] proposed micromechanically-based models adopting static hypothesis and were successfully used to simulate various behaviors of granular soils from sand to clay. More recently, [14] proposed a multi-scale modeling framework for granular media based on a hierarchical cross-scale. This framework is also implemented to simulate a variety of engineering problems including hydro-mechanical problems [15–17].

In this manuscript, a 3D micromechanically-based constitutive model named 3D-H model [45] is firstly implemented within an FEM code (ABAQUS) by using a multi-scale approach involving different scales spanning from microscale to macroscale. Each Gauss integration point in the finite element model represents a representative elementary volume (intermediate scale). The 3D-H model acts on the elementary cell, to relate both local strain and stress by taking the microstructure (microscopic scale) into account. Then, an experimental database on Ticino sand along drained triaxial loading path is used to calibrate the model parameters. Finally, a series of drained biaxial tests are performed to analyze the occurrence of strain localization by considering a plane-strain problem.

2. Constitutive formulations and schematic diagram

2.1. A review of the 3D-H model

The 3D-H model was developed from the micro-directional model [30], which was initially proposed to describe the mechanical behavior of snow [27] and then generalized to any type of granular assembly, with a particular emphasis on frictional granular materials [30]. Based on this approach, the H-model [28] was developed, replacing the notion of independent pairs of contacting particles by an intermediate granular assembly (the so-called granular hexagon, see Figure 3a), in which an enriched geometrical and kinematic description can be considered.

To build the stress-strain relation of granular media in 3D conditions, the coordinate transformation is implemented by employing the Euler angles

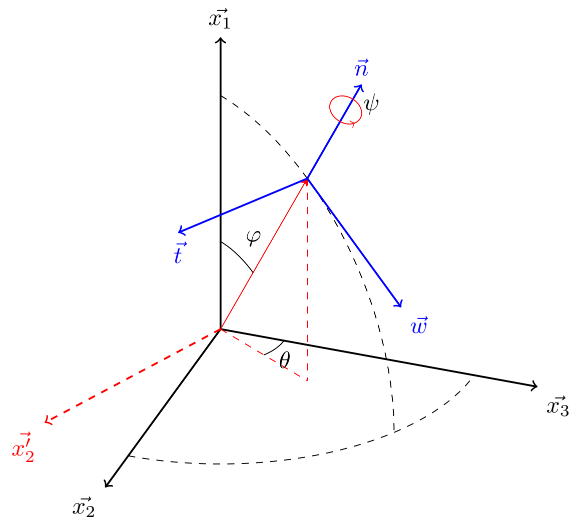

Figure 1: Global and local coordinate system transformation by employing Euler angles in 3D conditions.

(Figure 1). Then, the H-model was extended to 3D conditions, replacing the 2D hexagon with a 3D granular cluster (the so-called meso-structure, see Figure 3b). The 3D-H model [45] makes it possible to derive the macro-stress tensor from the macro-strain tensor according to the following steps:

(1) Kinematic localization: The meso-structure is a connection between macro-scale and meso-scale. The dimension of the meso-structure can be characterized by the vector: $\vec{L} = [l_1, l_2, l_3]^T$, wherein l_1, l_2, l_3 represent the lengths along directions $\vec{n}$, $\vec{t}$, $\vec{w}$, respectively. Thus, the kinematic localization assumption gives:

$$\delta \vec{L} = \bar{\bar{P}} \delta \bar{\bar{\varepsilon}} \bar{\bar{P}}^{-1} \vec{L} \tag{1}$$

where: $\delta\bar{\bar{\varepsilon}}$ is the incremental macro-strain tensor, $\bar{\bar{P}}$ is the rotation matrix from global frame $(\vec{x_1}, \vec{x_2}, \vec{x_3})$ to local frame $(\vec{n}, \vec{t}, \vec{w})$.

(2) Meso-structure behavior: The meso-structure (Figure 3b) can be de-

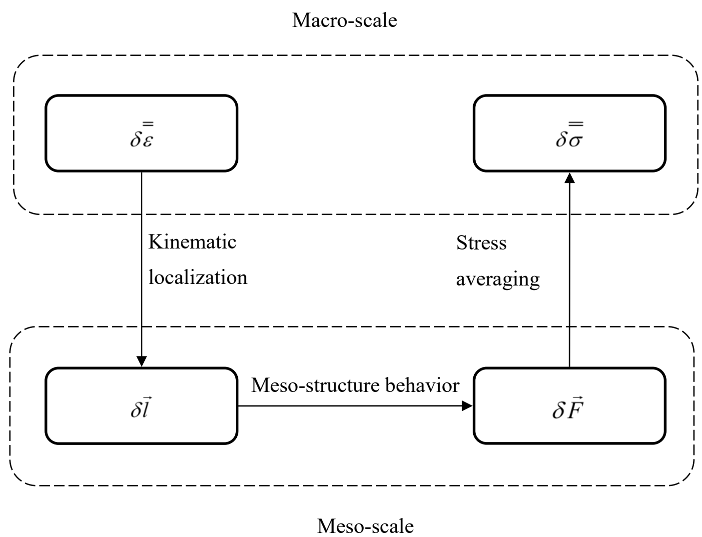

Figure 2: General homogenization scheme of 3D-H model [4].

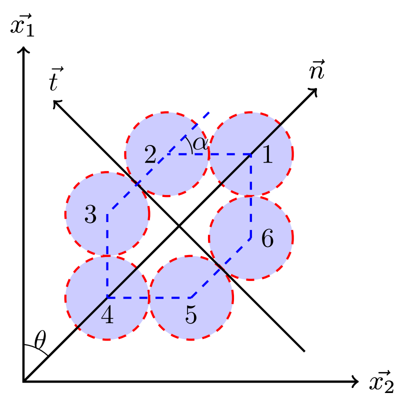

(a) The 2D hexagon in the H-model.

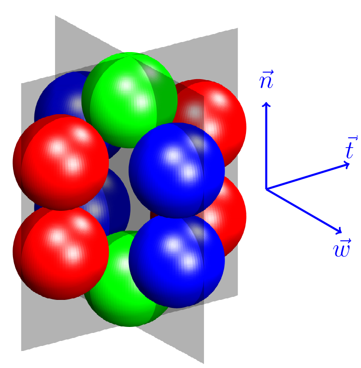

(b) The 3D meso-structure in the 3D-H model.

Figure 3: The granular assembly of the H-model and of the 3D-H model on the meso-scale.

composed into two independent hexagon patterns: Hexagon A (Figure 4) and Hexagon B (Figure 5). As shown in Figure 4a, the geometrical description for Hexagon A gives:

$$\begin{aligned} &\delta u_n^1 = \delta d_1 \\ &\delta u_t^1 = d_1 \delta\alpha_1 \\ &\delta u_n^2 = \delta d_2 \\ &l_1 = d_2 + 2d_1 \cos\alpha_1 \\ &l_2 = 2d_1 \sin\alpha_1 \end{aligned} \tag{2}$$

The force balance of grain 1 along direction $\vec{n}$ and of grain 2 along directions $\vec{w}$ and $\vec{n}$, together with the moment balance of grain 2 read:

$$\begin{aligned} &F_1^a = 2(N_1 \cos\alpha_1 + T_1 \sin\alpha_1) \\ &F_2 = N_1 \sin\alpha_1 - T_1 \cos\alpha_1 \\ &N_2 = N_1 \cos\alpha_1 + T_1 \sin\alpha_1 + G_2 \\ &G_2 = T_1 \end{aligned} \tag{3}$$

The elastic-perfect plastic inter-particle contact law reads:

$$\begin{aligned} &\delta N_c = k_n \delta u_n^c \\ &\delta\vec{T}_c = \min\left\{\left\|\vec{T}_c + k_t \delta\vec{u_t^c}\right\|, \tan\varphi_g\left(N_c + \delta N_c\right)\right\} \times \frac{\vec{T}_c + k_t\delta\vec{u_t^c}}{\left\|\vec{T}_c + k_t\delta\vec{u_t^c}\right\|} - \vec{T}_c \end{aligned} \tag{4}$$

Combining Equations (2) to (4) provides an equation relating $\delta\vec{l}$ and $\delta\vec{F^a}$. Similarly, the incremental constitutive relation for Hexagon B can also be obtained. Consequently, superimposing Hexagon A and Hexagon B, the total incremental force along direction $\vec{n}$ is $\delta\vec{F_1} = \delta\vec{F_1^a} + \delta\vec{F_1^b}$. The incremental constitutive relation of the 3D meso-structure is finally obtained.

(3) Stress averaging: Averaging the meso-stress taking place within all the meso-structures in the specimen of volume V can be performed as follows:

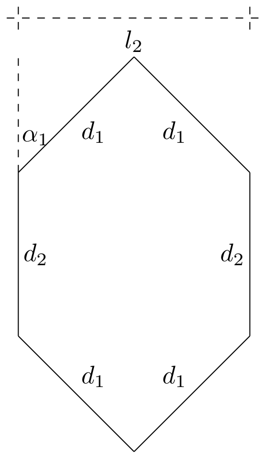

(a) Dimension of hexagon

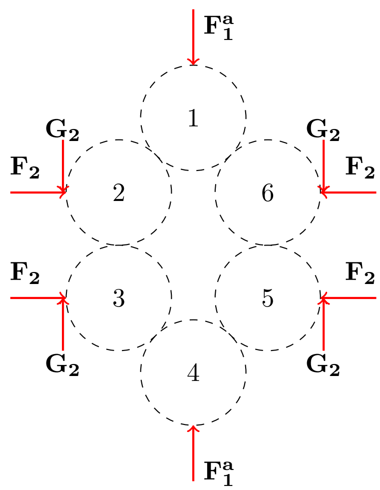

(b) External forces

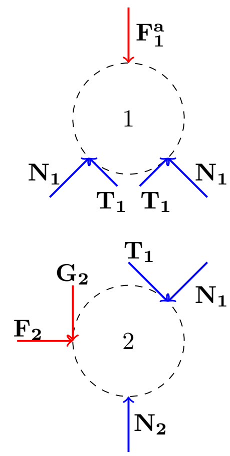

(c) Force balance for grains 1 and 2

Figure 4: Mechanical description of hexagon pattern A.

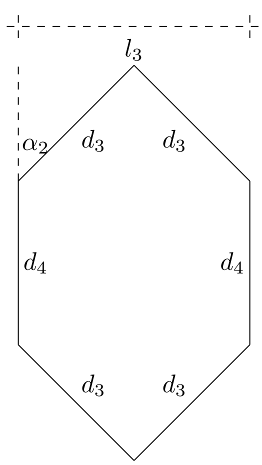

(a) Dimension of hexagon

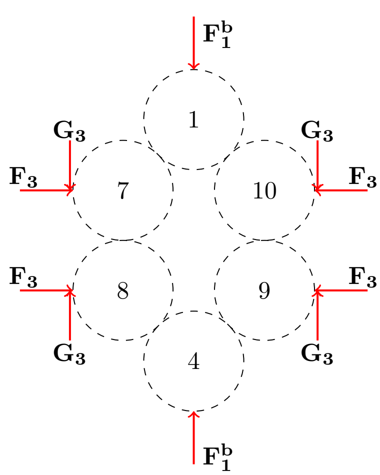

(b) External forces

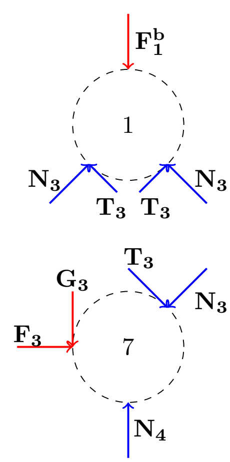

(c) Force balance for grains 1 and 7

Figure 5: Mechanical description of hexagon pattern B.

$$\bar{\bar{\sigma}} = \frac{1}{V} \iiint \omega(\theta, \varphi, \psi) \bar{\bar{P}}^{-1} \bar{\bar{\tilde{\sigma}}}(\vec{n}, \vec{t}, \vec{w}) \bar{\bar{P}} \sin\varphi d\varphi d\theta d\psi \tag{5}$$

where $\bar{\bar{\sigma}}$ is the macro-stress tensor operating on the specimen scale. For an isotropic specimen, the distribution function $\omega(\theta, \varphi, \psi)$ is constant and $\theta \in [0, 2\pi[, \varphi \in [0, \pi], \psi \in [0, 2\pi[$ (θ, φ, ψ are the Euler angles). The meso-stress $\bar{\bar{\tilde{\sigma}}}(\vec{n}, \vec{t}, \vec{w})$ with respect to the local frame can be computed from the local variables using the Love's formula [7, 11, 22, 23]:

$$\begin{aligned}
\widetilde{\sigma}_{11}(\vec{n}, \vec{t}, \vec{w}) &= 4N_1 d_1 \cos^2\alpha_1 + 4T_1 d_1 \cos\alpha_1 \sin\alpha_1 + 2N_2 d_2 \\
&\quad +4N_3 d_3 \cos^2\alpha_2 + 4T_3 d_3 \cos\alpha_2 \sin\alpha_2 + 2N_4 d_4 \\
\widetilde{\sigma}_{22}(\vec{n}, \vec{t}, \vec{w}) &= 4N_1 d_1 \sin^2\alpha_1 - 4T_1 d_1 \cos\alpha_1 \sin\alpha_1 \\
\widetilde{\sigma}_{33}(\vec{n}, \vec{t}, \vec{w}) &= 4N_3 d_3 \sin^2\alpha_2 - 4T_3 d_3 \cos\alpha_2 \sin\alpha_2 \\
\widetilde{\sigma}_{ij}(\vec{n}, \vec{t}, \vec{w}) &= 0 \quad \text{when} \quad i \neq j
\end{aligned} \tag{6}$$

The principal components of meso-stress tensor are calculated from the internal forces acting within the meso-structure. Besides, off-diagonal components can be simply considered as nil, because the meso-structure with respect to $(\vec{n}, \vec{t}, \vec{w})$ always offsets the one with respect to $(-\vec{n}, -\vec{t}, -\vec{w})$ in off-diagonal components when integrated.

2.2. Finite element formulation

The FEM code (ABAQUS/Explicit) [20] is used to solve BVPs in the context of this multi-scale approach. An arbitrary geometric domain Ω of a given BVP is firstly discretized into apposite FEM meshes with geometric position $\vec{x}$. The discretized equilibrium equation for the whole mesh reads:

$$\vec{F^e} - \vec{F^i} = \bar{\bar{M}} \vec{\ddot{u}} \tag{7}$$

where $\vec{F^e}$ is the external force vector; $\vec{F^i}$ is the internal force vector; $\bar{\bar{M}}$ is the mass matrix and $\vec{u}$ is the displacement of each material point $\vec{x}$.

The internal force vector is given by:

$$\vec{F^i} = \bar{\bar{K}}\vec{u} \tag{8}$$

where $\bar{\bar{K}}$ is the stiffness matrix, calculated from the 3D-H model (constitutive relation) and the interpolation assumption (geometric relation) in the element.

Thus, for a dynamic equilibrium state at the current time (t):

$$\bar{\bar{M}}\vec{\ddot{u}}|_t = (\vec{F^e} - \vec{F^i})|_t \tag{9}$$

The central difference integration scheme is used to update velocities and displacements:

$$\begin{cases} \vec{\dot{u}}|_{(t+\frac{\Delta t}{2})} & = & \vec{\dot{u}}|_{(t-\frac{\Delta t}{2})} + \left(\frac{\Delta t|_{(t+\Delta t)}+\Delta t|_t}{2}\right)\vec{\ddot{u}}|_t \\ \vec{u}|_{(t+\frac{\Delta t}{2})} & = & \vec{u}|_t + \Delta t|_{(t+\Delta t)}\vec{\dot{u}}|_{(t+\frac{\Delta t}{2})} \end{cases} \tag{10}$$

The geometry is updated by adding the displacement increments to the initial geometrical configuration $\vec{x}_0$:

$$\vec{x}_{t+\Delta t} = \vec{x}_0 + \vec{u}_{t+\Delta t} \tag{11}$$

When presenting the numerical results throughout this paper, the convention in soil mechanics which treats compression as positive is followed. In 2D conditions, two commonly referred stress measurements the mean stress p and the deviatoric stress q can be calculated based on the Cauchy stress tensor $\bar{\bar{\sigma}}$ as:

$$
\begin{aligned}
p &= \tfrac{1}{3}\mathrm{tr}\bar{\bar{\sigma}} \\
q &= \sqrt{\tfrac{3}{2}\bar{\bar{\sigma}}_{dev} : \bar{\bar{\sigma}}_{dev}}
\end{aligned} \tag{12}
$$

where $\bar{\bar{\sigma}}_{dev}$ is the deviatoric stress tensor, $\bar{\bar{\sigma}}_{dev} = \bar{\bar{\sigma}} - p\bar{\bar{\delta}}$, with $\bar{\bar{\delta}}$ being the Kronecker symbol.

The volumetric strain ε_v and the deviatoric strain ε_q can be derived as:

$$
\begin{aligned}
\varepsilon_v &= \mathrm{tr}\bar{\bar{\varepsilon}} \\
\varepsilon_q &= \sqrt{\tfrac{2}{3}\bar{\bar{\varepsilon}}_{dev} : \bar{\bar{\varepsilon}}_{dev}}
\end{aligned} \tag{13}
$$

where $\bar{\bar{\varepsilon}}_{dev}$ is the deviatoric strain tensor, $\bar{\bar{\varepsilon}}_{dev} = \bar{\bar{\varepsilon}} - \frac{1}{3}\varepsilon_v\bar{\bar{\delta}}$.

2.3. Multi-scale approach implementation

The FEM implementation of the 3D-H model constitutes a complete multi-scale procedure. In FEM, the cell is usually called 'microscale' due to the fact that it is one of the fundamental elements of a BVP. However, this cell can also be called 'macroscale', because it is the REV (representative elementary volume) in DEM. To clarify, different scales involved in this multi-scale approach are depicted in Figure 7. Gauss integration points in the FEM mesh correspond to the REV scale at which the 3D-H model operates. Two intermediate scales (hexagon scale and REV scale) are introduced to bridge macro and micro scales. The element type named C3D8R (three-dimensional eight-node brick element with reduced integration) is selected. The schematic diagram of the framework is depicted in Figure 6 and can be illustrated by the following steps:

(1) From macro-scale to the REV scale, the BVP is solved by using ABAQUS dynamic-explicit solver. The macro-strain of each element is computed, and then transferred to the REV scale.

(2) From the REV scale to the meso-scale, the 3D-H model is employed. The macro-strain is distributed to local meso-structures by using kinematic localization (Equation 1). Thus, the strain of the meso-structure is obtained.

(3) From the meso-scale to the REV scale, the constitutive relation of the meso-structure is firstly obtained, then the internal forces within the meso-structure are calculated. By using Love's formula, the stress within the REV is calculated.

(4) From the REV scale to the macro-scale, the macro-stress is computed after all the stresses acting at integration points are calculated.

3. Finite element model and benchmark

3.1. Finite element model

In order to examine the performance of the multiscale approach elaborated in previous section, the numerical analysis presented in this paper mainly focuses on triaxial compression loading under the plane-strain condition. As shown in Figure 8, the specimen with size: $0.2(\vec{x_1})\times 0.1(\vec{x_2})\times 0.005$ $(\vec{x_3})$ m^3 is assembled between two rigid bars. The degree of freedom along $\vec{x_3}$ of the whole model is blocked while the confining stress is applied along $\vec{x_2}$.

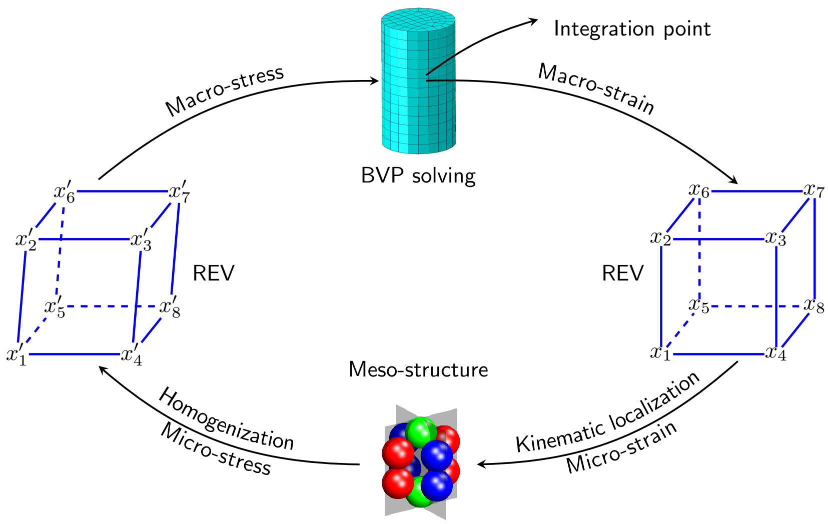

Figure 6: The schematic diagram of multi-scale approach based on the 3D H-model.

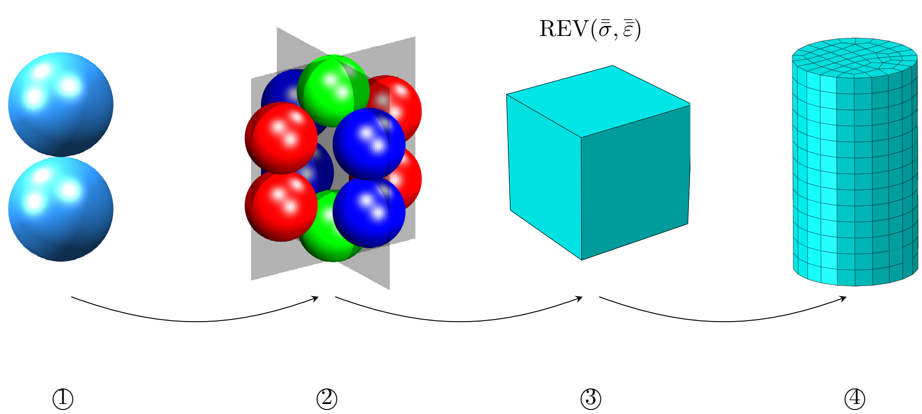

①: contact scale (microscale)
②: hexagon scale
③: REV scale
④: BVP scale (macroscale)

intermediate scales

Figure 7: Different scales involved in the multi-scale approach.

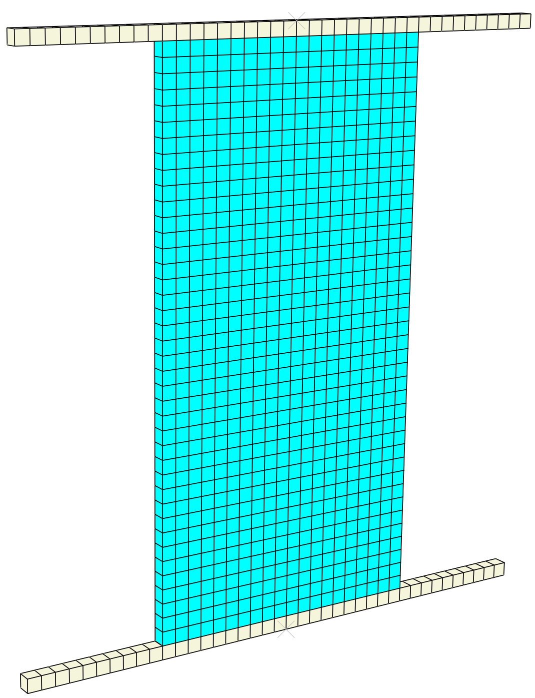

(a) Model perspective view

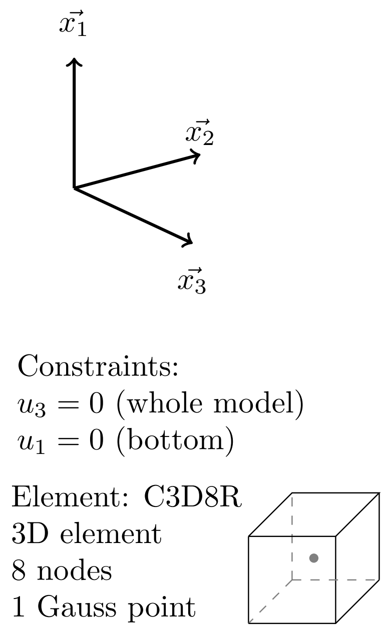

(b) Constraints and element type.

Figure 8: Model constraints and element type.

3.2. Calibration and verification

In relation with the elastic-perfect plastic inter-particle contact law, it is worth noting that this multiscale approach involves only three material parameters and one micro geometrical parameter. The formers including the normal stiffness (k_n), tangential stiffness (k_t), inter-particle friction angle (φ_g) stem from the contact law, while the latter is the opening angle (α_0) calculated from the initial void ratio. Thus, four parameters need to be calibrated. These parameters are determined by trial and error in order to provide the best fit to a single isotropically compressed drained triaxial test confined at 200 kPa on Ticino sand with $D_R = 74\%$ of relative density. The best fit of $D_R = 74\%$ is shown in Figure 9 while the employed parameters are reported in Table 1. Afterwards, these parameters are used to examine the model predictive capability by comparing the experimental data from the drained triaxial test confined at 100 kPa and 300 kPa. The results are observed in Figure 9, where the predicted curves are in agreement with the experimental curves.

Table 1: Parameters selected in calibration and prediction phases

k_n/r_g(Pa)	k_t/k_n	e_0	$\varphi_g(°)$
1.90×10^9	0.6	0.53	25

3.3. Mesh dependency

In order to assess the sensitivity of finite element mesh for the localization analysis, five cubic mesh patterns with different elements are considered.

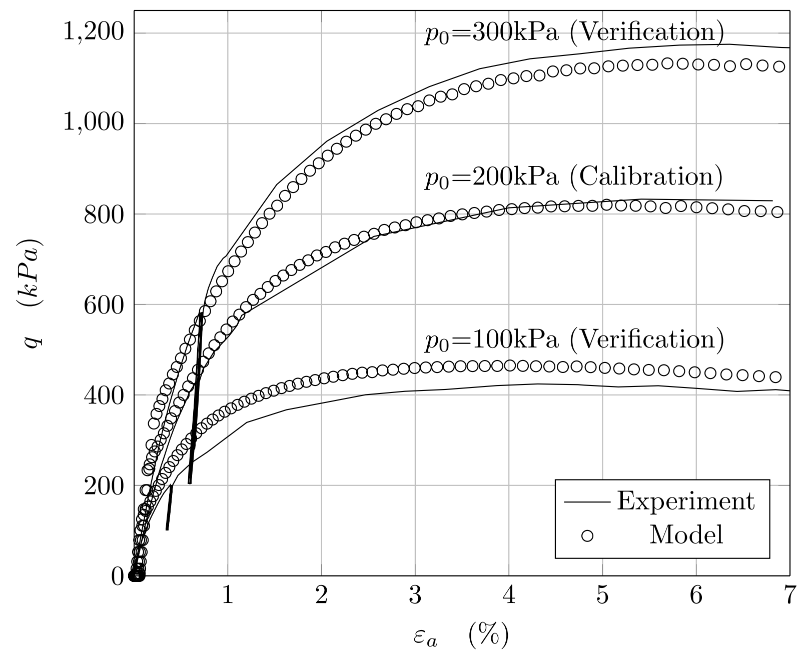

(a) Mechanical response.

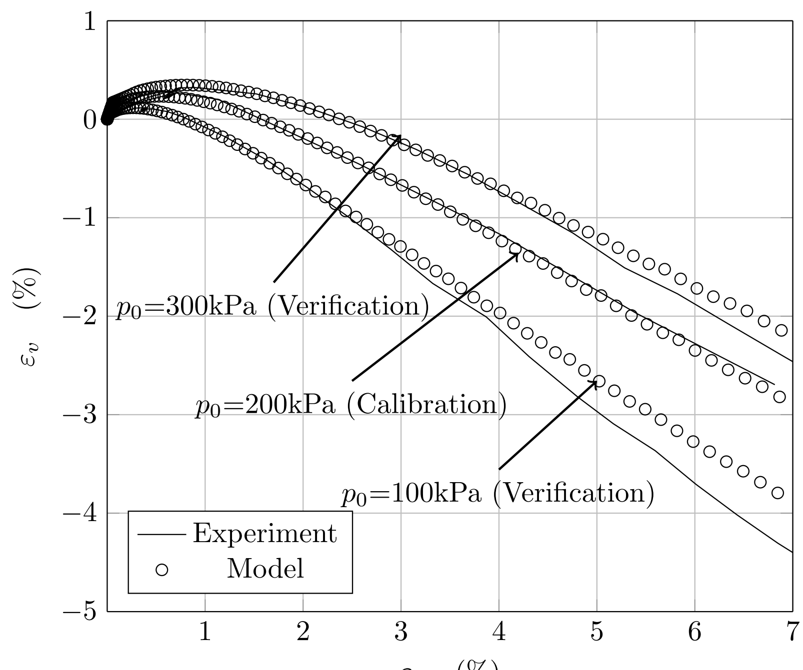

(b) Volumetric response.

Figure 9: Parameters calibration and model verification using the triaxial compression test on Ticino sand ($D_R = 74\%$).

Figure 10 and Figure 11 show the mechanical responses and volumetric responses for all the mesh patterns along drained triaxial loading paths at 200 kPa of confining stress. It is remarkable that whatever the mesh is, the hardening phase is the same ($\varepsilon_a < 3.6\%$). Afterwards, the curves reach the stress peak, and a softening behavior can be observed, where the more elements are used, the deeper the deviatoric stress drops. The softening phase reveals a mesh dependency stemming from the strain localization. As shown in Figure 12, no visible strain localization can be observed with 50 elements and 200 elements, whereas it evidently exists with 406 elements, 595 elements, 800 elements and 1653 elements. Due to the strain localization, a given increment of top loading displacement is no longer accommodated by all the elements in the whole specimen, but localized through a much marked shear deformation in the band. However, the different curves tend toward a unique one when the number of elements is increased. Besides, taking into account the computational efficiency, the mesh with 800 elements is used hereafter. Note that this length scale issue can be circumvented by different ways [21, 43].

4. Drained triaxial tests

The plane-strain model with 800 elements is used to investigate the strain localization problem. As discussed in the previous section, the calibrated parameters listed in Table 1 are adopted. A series of tests described in Table 2 and Table 3 are performed to analyze the model performance under drained triaxial loading paths. The effects of boundary conditions (T1-T4) and imperfection positions (T5-T8) are firstly investigated. Then, test T1

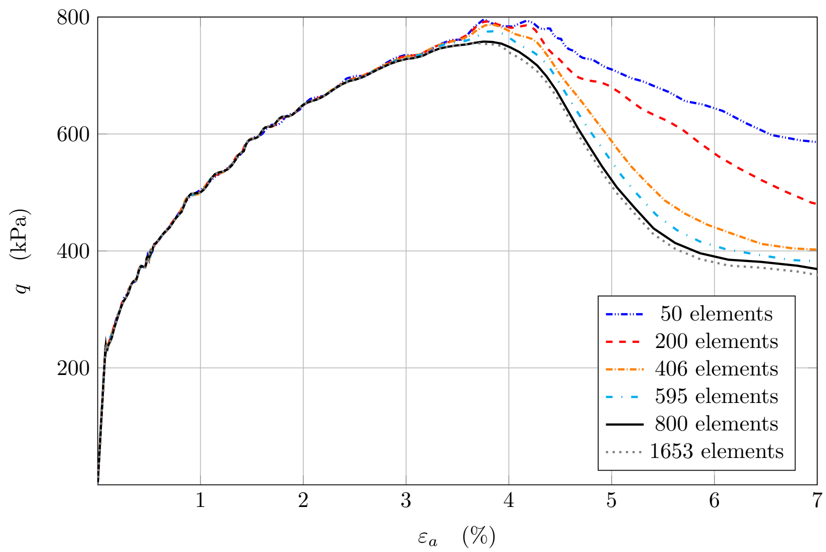

Figure 10: Mechanical response with different mesh patterns under the drained triaxial loading path at 200 kPa of confining stress.

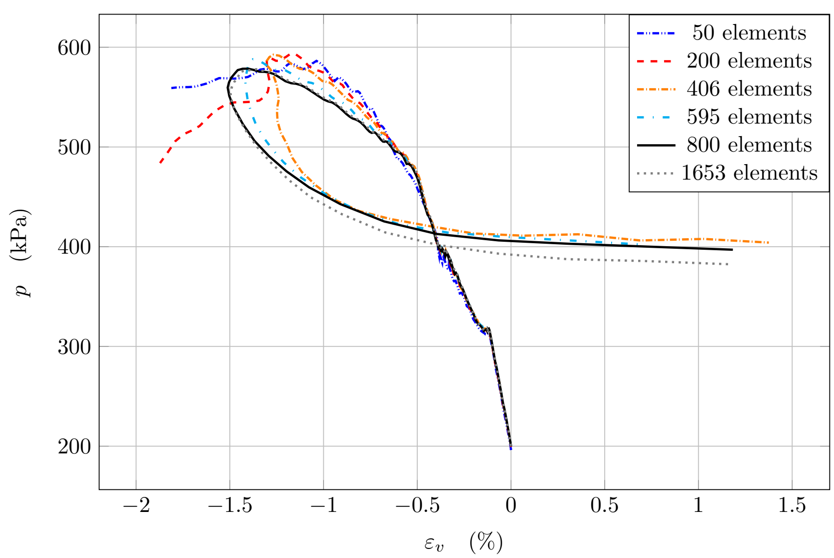

Figure 11: Volumetric strain versus mean stress with different mesh patterns under the drained triaxial loading path at 200 kPa of confining stress.

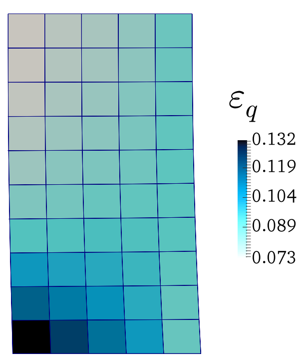

(a) 50 elements

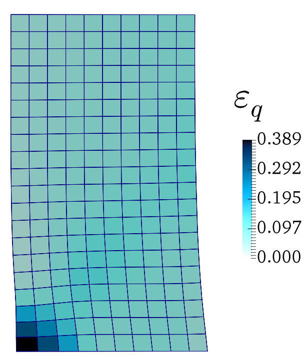

(b) 200 elements

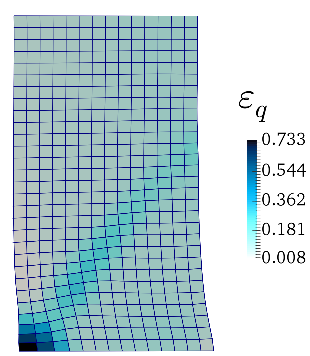

(c) 406 elements

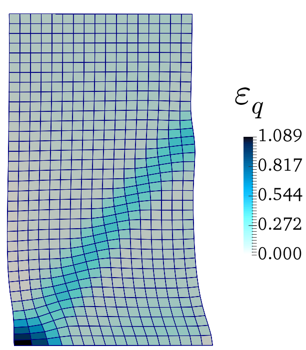

(d) 595 elements

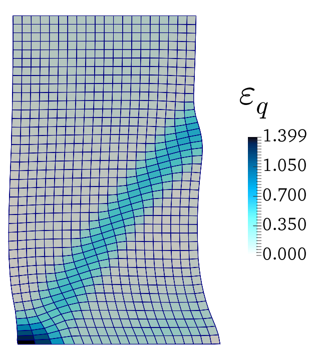

(e) 800 elements

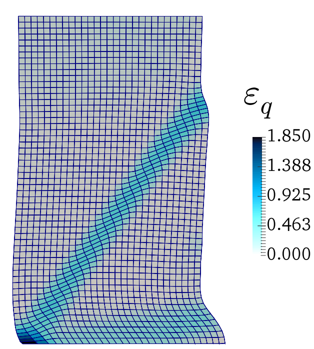

(f) 1653 elements

Figure 12: Contours plotting of deviatoric strain ε_q for the deformed configuration at the state of axial strain $\varepsilon_a = 6\%$.

is considered as a representative test to discuss the influence of initial void ratio and confining stress.

Test	**Imperfection position**	**Boundary condition**
T1	None	①
T2	None	②
T3	None	③
T4	None	④
T5	①	②
T6	②	②
T7	③	②
T8	④	②

Table 2: Imperfection positions and boundary conditions of different tests, further explanations are supplied in Table 3.

	① ② ③ ④
Boundary condition	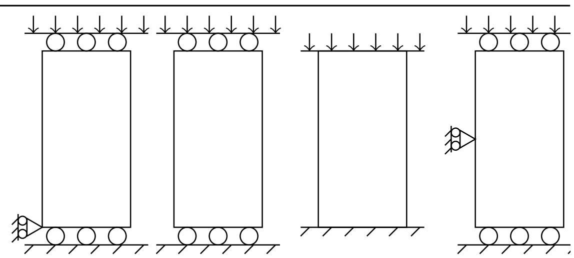
Imperfection position	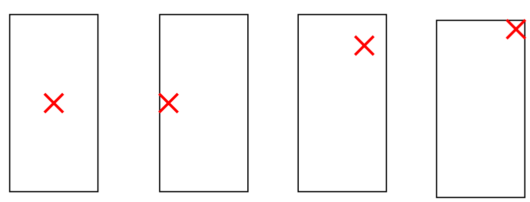

Table 3: Schematic diagram of imperfection positions and boundary conditions given in Table 2.

4.1. Model performance

Figure 13 compares the numerical results in terms of deformed configuration and strain field ε_q for different boundary conditions (T1-T4). By the same token, strain localization with inclined shear band(s) appear(s) in all tests (T1-T4) even though symmetrical boundary conditions (T2 and T3) are adopted. For non-symmetric boundary conditions, the strain localization normally initiates from the non-symmetric boundary point, gradually penetrates the whole specimen to form shear band(s). However, if the boundary conditions do not break the symmetry, the elements on the corner firstly reach stress peak and then shear bands develop.

An initial imperfection is introduced in the specimen via some material perturbation in terms of increasing initial void ratio from $e = 0.53$ to $e = 0.54$. The imperfection positions are depicted in Table 3. Figure 14 compares the failure patterns on deformed configurations in terms ε_q for distinct imperfection positions. Particularly, even though the material and boundary conditions are homogeneous, the strain localization can be still observed. The deformed configurations referring to distinct imperfection positions are totally different. Generally speaking, shear bands are usually centered on the material point with imperfection. The shape of strain localization depends on the imperfection position: X-shape shear band (T5), half X-shape shear band (T6) or quarter X-shape shear band (T7, T8).

Initiation and development of strain localization are governed by different mechanisms: they do not depend only on boundary conditions and material imperfections, but are also affected by the initial void ratio and confining stress [13]. In this section, the effects of initial void ratio and confining

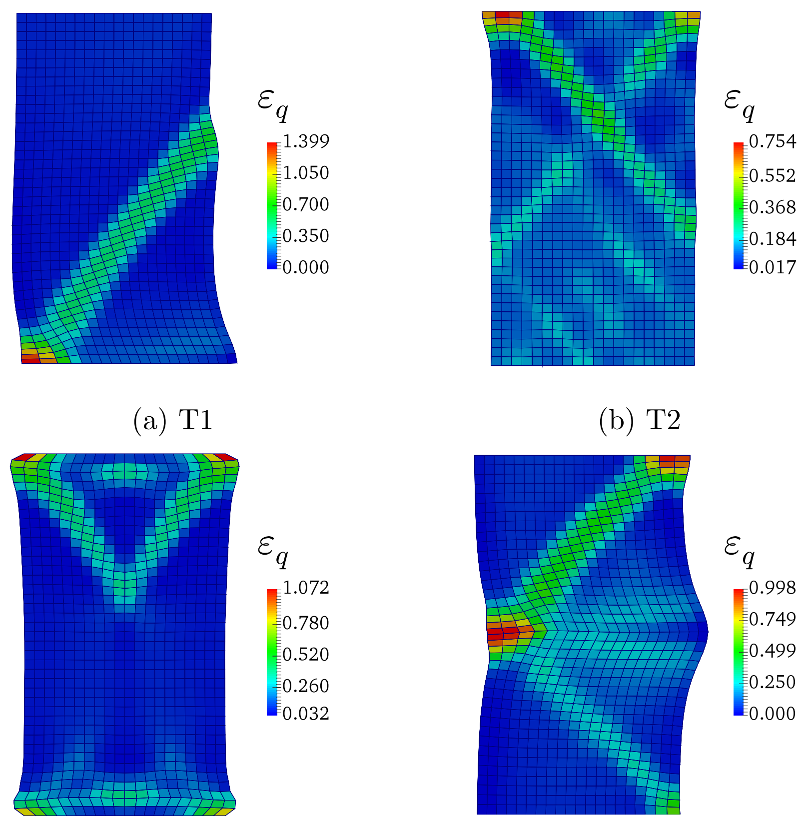

(a) T1 (b) T2

(c) T3 (d) T4

Figure 13: Failure patterns on deformed configuration in terms of ε_q for distinct boundary conditions (T1-T4).

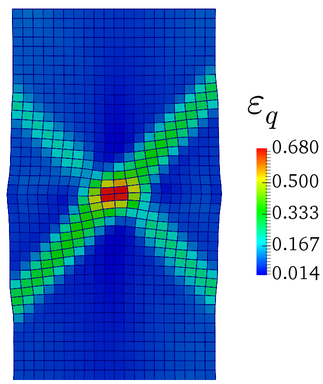

(a) T5

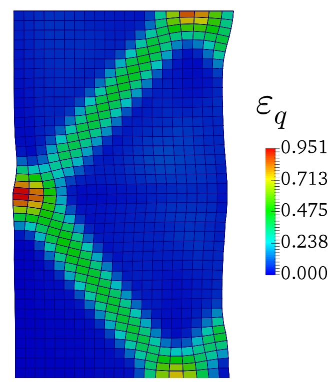

(b) T6

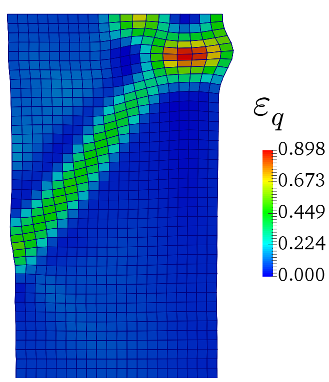

(c) T7

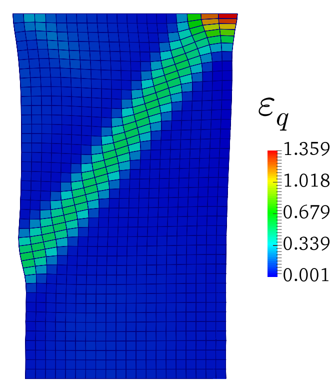

(d) T8

Figure 14: Failure patterns on deformed configuration in terms of ε_q for distinct imperfection positions (T5-T8).

stress are numerically analyzed under plane strain conditions. Figure 15 and Figure 16 show the mechanical response of the specimen, together with failure patterns at different confining stress for test T1. It is worth noting that the initiation of strain localization corresponds to the stress peak of the mechanical response. The plots clearly demonstrate the influence of confining stress on the mechanical response. The stress peak is reached faster, which means that the strain localization initiates earlier, when the specimen is subjected to lower confining stress compared to those confined at higher stress. It is consistent with the experimental results observed by [1, 19].

The dense homogeneous specimens for test T1 with initial void ratio spanning from 0.53 to 0.63 are subjected to the triaxial loading path, confined at 200 kPa. Figure 17 shows the evolution of deviatoric stress versus overall axial strain. It is observed that the looser the specimen is, the earlier the strain localization initiates, because the stress peak of the looser specimen is reached at a lower axial strain and then the looser specimen becomes heterogeneous.

It is worth noting that the shear band inclination, θ, is in good agreement with the values given by Roscoe's approximation: $\theta = \pi/4 + (\varphi_m + \psi_m)/4$, where φ_m is mobilized friction angle and ψ_m is dilatancy angle. For the 3D-H model, the micro friction angle $\varphi_m = \varphi_g = 25.00°$ and the dilatancy angle $\psi_m = 1.00°$ is measured in Figure 17b. Thus, $\theta = 45.00° + (25.00° + 1.00°)/4 = 51.50°$ which is exactly measured in Figure 18a. Note that material parameters can also affect the shear banding, as demonstrated by [44].

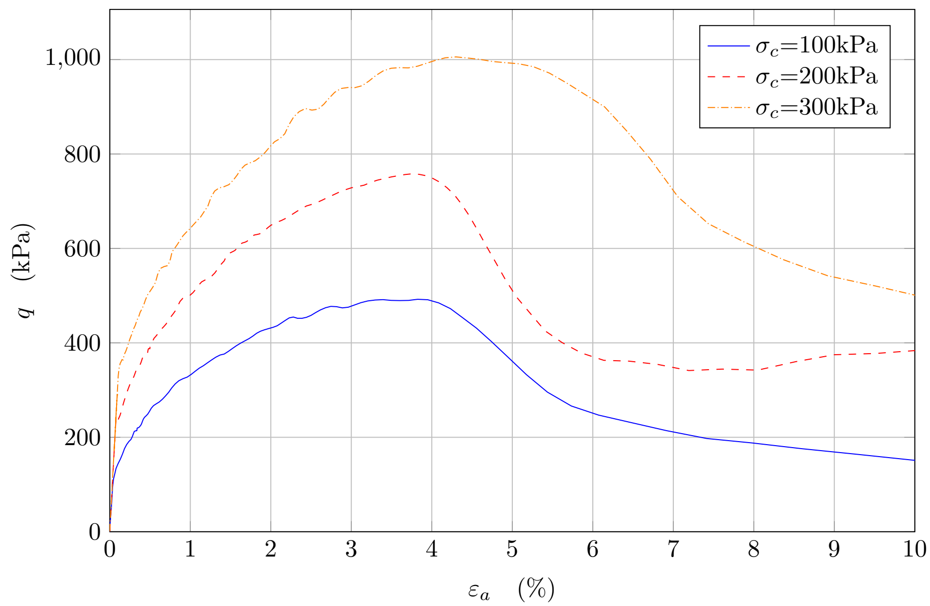

Figure 15: Mechanical response with different confining stresses for test T1.

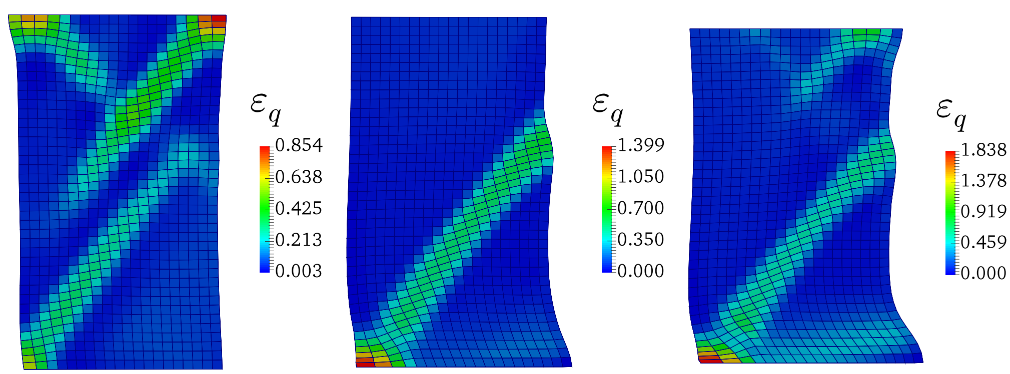

(a) $\sigma_c = 100$kPa (b) $\sigma_c = 200$kPa (c) $\sigma_c = 300$kPa

Figure 16: Failure patterns on deformed configuration in terms of ε_q for different confining stresses in test T1.

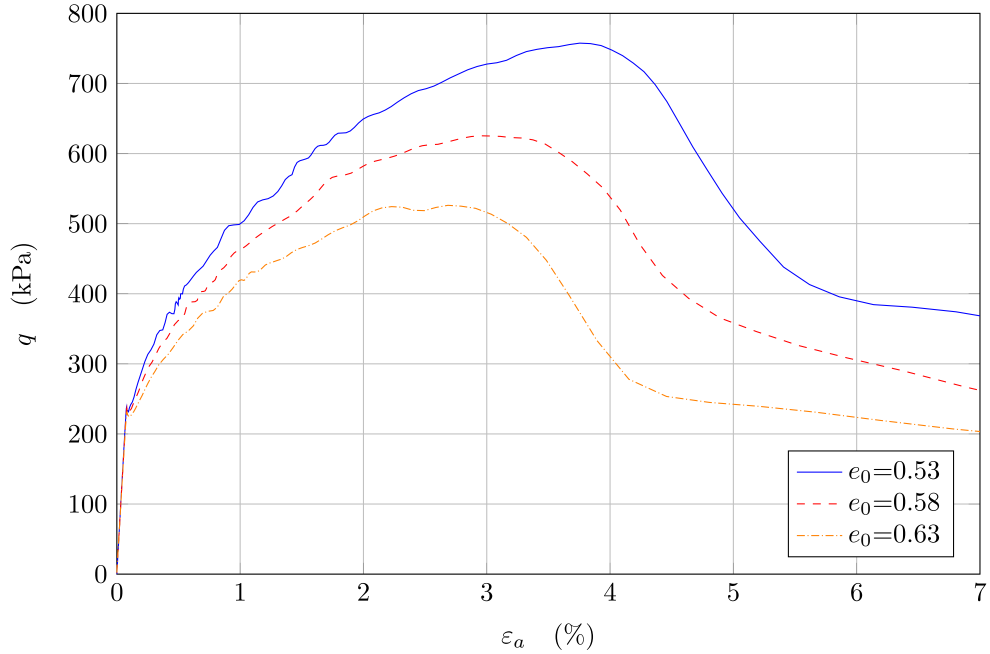

(a) Mechanical response.

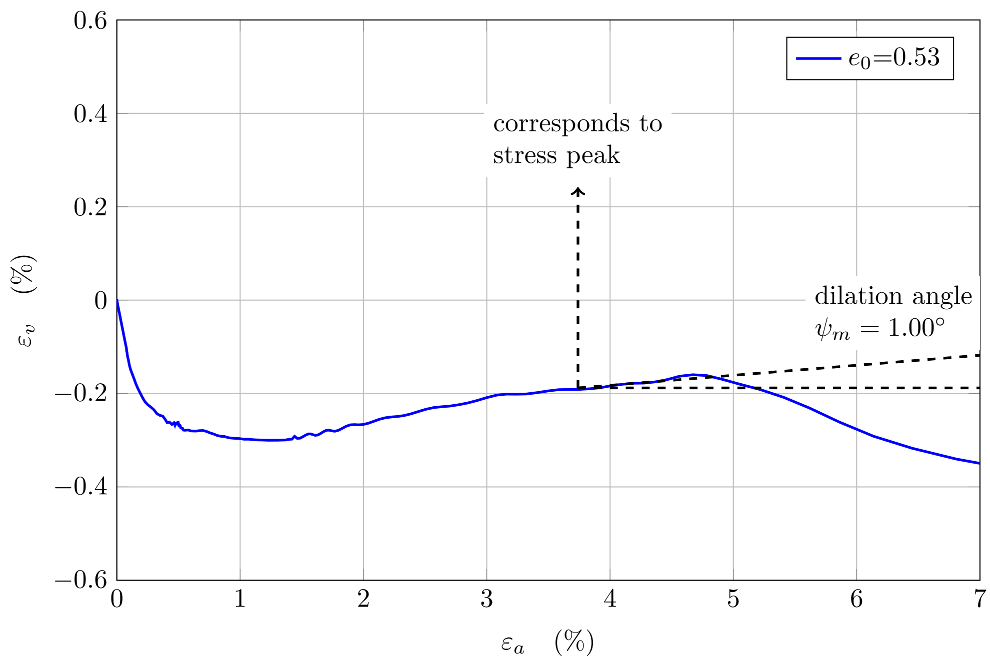

(b) Volumetric responses.

Figure 17: Mechanical and volumetric responses with different initial void ratios for test T1.

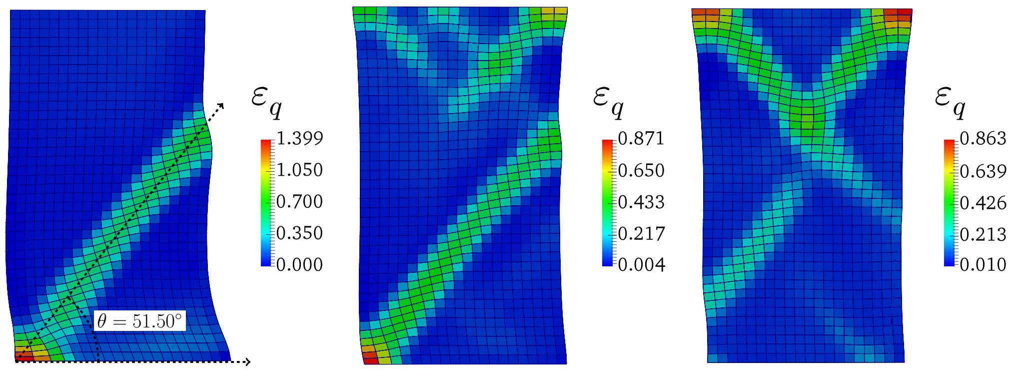

(a) $e = 0.53$ (b) $e = 0.58$ (c) $e = 0.63$

Figure 18: Failure patterns on deformed configuration in terms of ε_q for different initial void ratios in test T1.

4.2. Phases transition: from homogeneity to inhomogeneity

The nature of the mechanical response of a perfectly homogeneous specimen is investigated in this section. The parameters and initial conditions are identical for all elements in the mesh. Figure 19a and Figure 19b show the mechanical responses and volumetric responses for all the elements in the finite element mesh, respectively. The first remark is that from the beginning to the line ①, whatever the mechanical response (stress or volumetric response), the specimen behaves perfectly homogeneously corresponding to the purely elastic regime of the model. The curves approximately coincide from lines ① to ② with slight differences due to possible dynamical effects. All curves bifurcate at a bifurcation point (line ②), which occurs at around 4% of axial strain indicating the loss of uniqueness of solutions of BVPs as a homogeneous problem. This loss of uniqueness corresponds to the violation of Rice's criterion [10, 33, 37, 42].

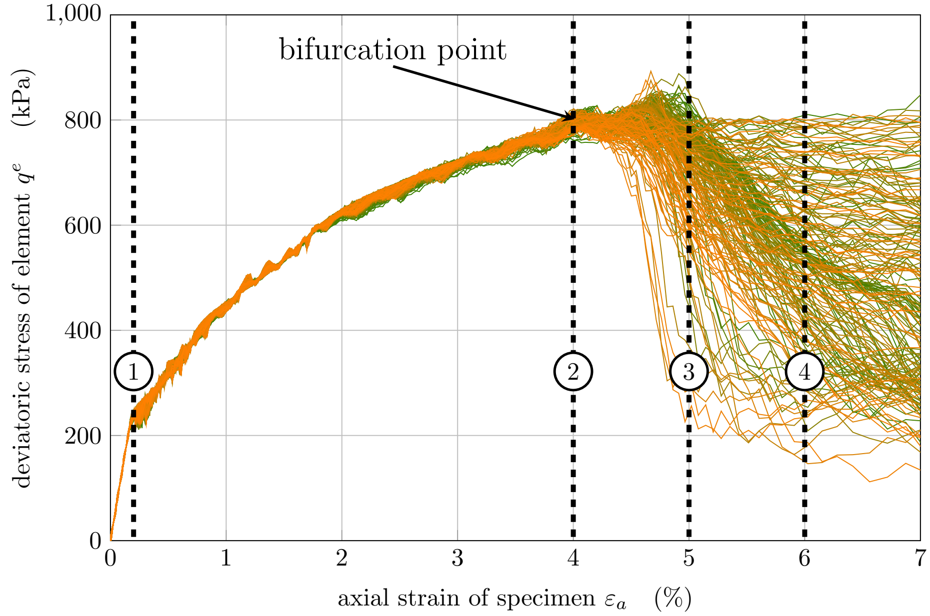

(a) Deviatoric stress of each element versus specimen axial strain.

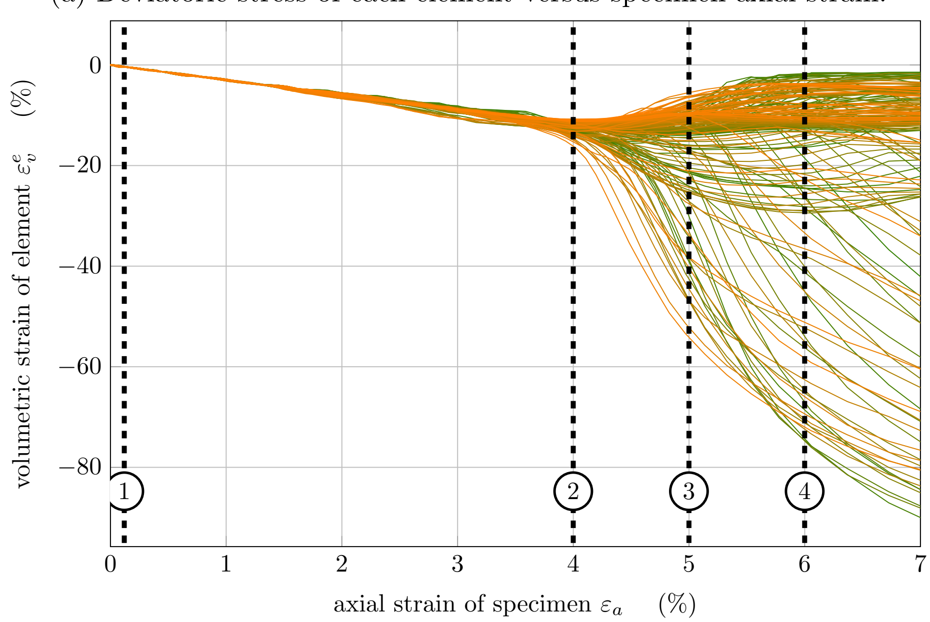

(b) Volumetric strain of each element versus specimen axial strain.

Figure 19: Mechanical and volumetric responses for all elements in the mesh.

Figure 20 shows the maps of normalized second-order work W_{2n} for the deformed configuration at three different states corresponding to lines ②, ③ and ④ in Figure 19. The second-order work for each element can be normalized as follows:

$$W_{2n} = \frac{\delta\bar{\bar{\sigma}} : \delta\bar{\bar{\varepsilon}}}{\parallel \delta\bar{\bar{\sigma}} \parallel \parallel \delta\bar{\bar{\varepsilon}} \parallel} \tag{14}$$

As shown at state ② in Figure 20, the negative values of W_{2n} distribute in the whole specimen, indicating the unstable state of most of the elements, which corresponds to the bifurcation point reported in Figure 19. After that, at states ③ and ④, the negative values of W_{2n} concentrate in a narrow zone: a shear band naturally and gradually appears. The material points located inside the shear band remain unstable as negative second-order work values subsist, whereas other points outside the shear band undergo unloading with positive values of second-order work. It is noted that the bottom area of the specimen also reveals negative values at state ② due to the fact that the non-symmetry of the boundary conditions leads to horizontal displacements. However, it gradually disappears when the shear band becomes evident at state ③.

Figure 21 correspondingly shows the maps of kinetic energy E_k (J) for the deformed configuration at states ②, ③ and ④. At the bifurcation point ②, elements on the left and bottom boundary firstly experience an increase in kinetic energy due to the deformation of the elements at the bottom left corner. After the shear band appears, the specimen is divided into two parts. The top part evolves in a dynamic regime directed by the external displacement loading applied at the top of the specimen, whereas the bottom part only experiences a material dilatancy. It is consistent with previous work of [13, 36]

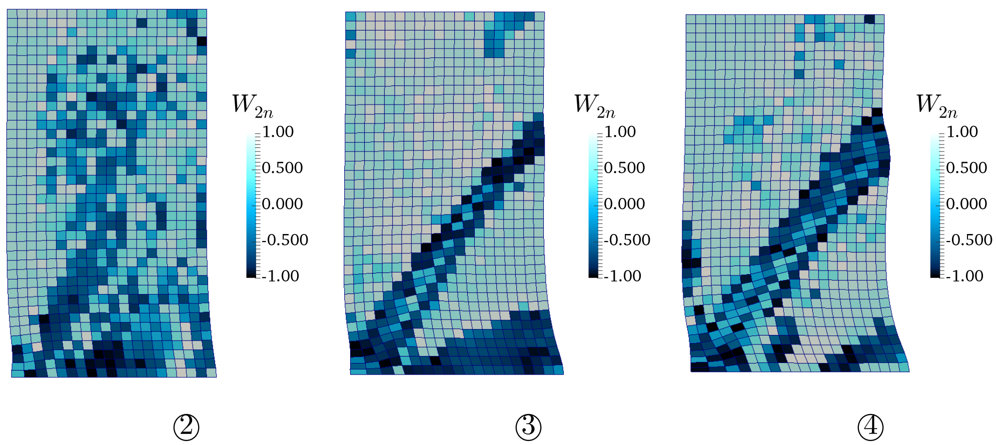

Figure 20: The maps of normalized second-order work W_{2n} for the deformed configuration at different states (see Figure 19).

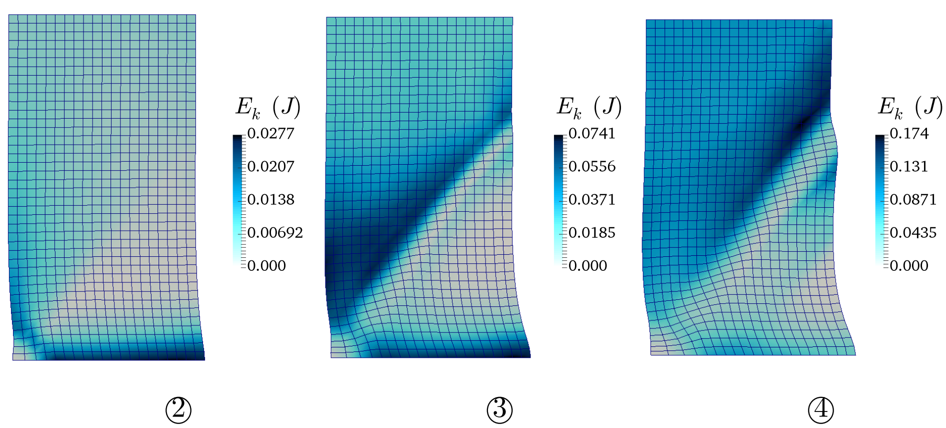

Figure 21: The maps of kinetic energy E_k (J) for the deformed configuration at different states corresponding to Figure 19.

4.3. Inside and outside shear band

As illustrated in the previous section, the specimen loses homogeneity when the shear band appears. Thus, the specimen can be considered as constituted with two parts: inside shear band area and outside shear band area. The material behavior should be analyzed separately in these two regions.

A shear band or, more generally, a strain localization refers to a special zone where the strain largely concentrates, usually of plastic nature, and develops during large deformation of the material. For test T1, based on the map of deviatoric strain (Figure 22a), inside shear band area and outside shear band area are separated as shown in Figure 22b.

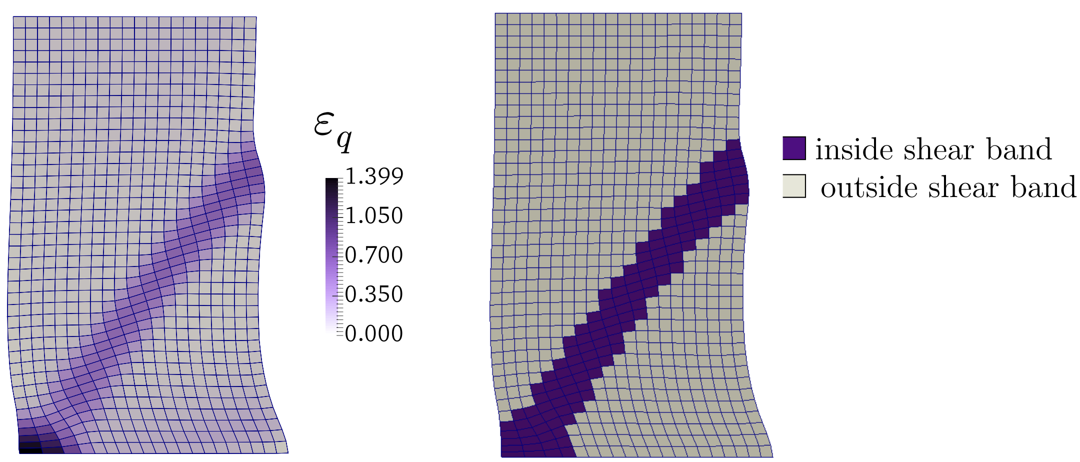

(a) The map of ε_q for the deformed configuration of T1 at the strain $\varepsilon_a = 6\%$.

(b) Determination of inside shear band area and outside shear band areas.

Figure 22: Shear band area definition.

Figure 23a shows the evolution of volumetric strain with respect to the overall axial strain for specimen T1: inside shear band area, outside shear band area and total area. The three curves are coinciding before $\varepsilon_a = 4\%$ due to the fact that the specimen is homogeneous. However, the inside shear band curve and outside shear band curve diverge toward two different states after $\varepsilon_a = 4\%$. The outside shear band curve becomes more contractant whereas the inside shear band curve shows dilatancy. Moreover, the global curve does not allow to figure out the strong dilatancy taking place within the shear band. Figure 23b correspondingly shows the evolution of second-order work against the overall axial strain for specimen T1. The inside shear band second-order work (W_2^{in}) and the outside shear band second-order work (W_2^{out}) are computed as follows:

$$\begin{aligned} W_2^{in} &= \sum_{i \in \text{inside}} \left(\delta\bar{\bar{\sigma}}^i : \delta\bar{\bar{\varepsilon}}^i \right) \\ W_2^{out} &= \sum_{i \in \text{outside}} \left(\delta\bar{\bar{\sigma}}^i : \delta\bar{\bar{\varepsilon}}^i \right) \end{aligned} \tag{15}$$

Similar to the volumetric strain curve, the inside shear band second-order work (W_2^{in}) and the outside shear band second-order work (W_2^{out}) diverge when the shear band appears. W_2^{in} shows a significant decreasing dropping to negative values whereas the W_2^{out} stays positive. It should be noted that the number of elements inside the shear band is much less than the number of elements outside the shear band. Finally, this result recovers the fact that the material response and the underpinning mechanisms are totally different inside shear band area and outside shear band area [12, 39, 50].

Figure 24 reveals the microscopic variable distributions at Gauss points inside and outside shear band for specimen T1 at the state of $\varepsilon_a = 6\%$. For the sake of simplification, the mesostress is integrated over θ and ψ as

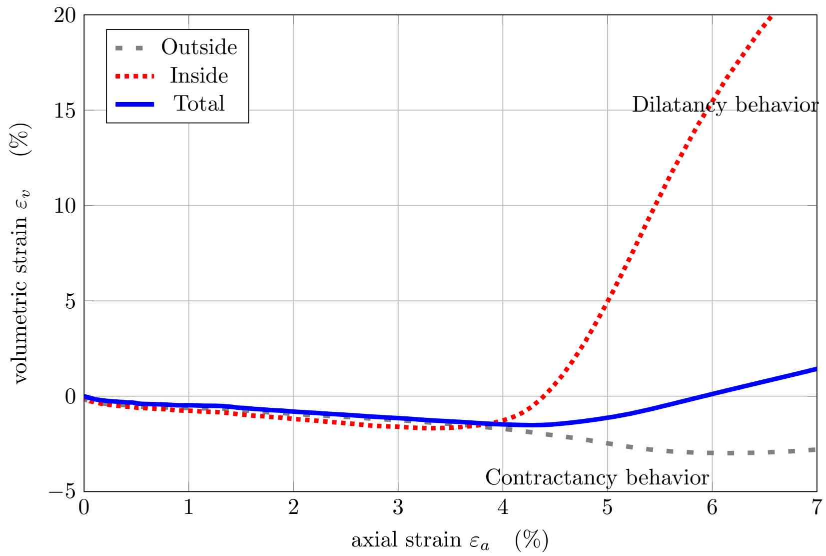

(a) Evolution of the volumetric strain ε_v (%) against the overall axial strain ε_a (%): inside shear band, outside shear band and total area.

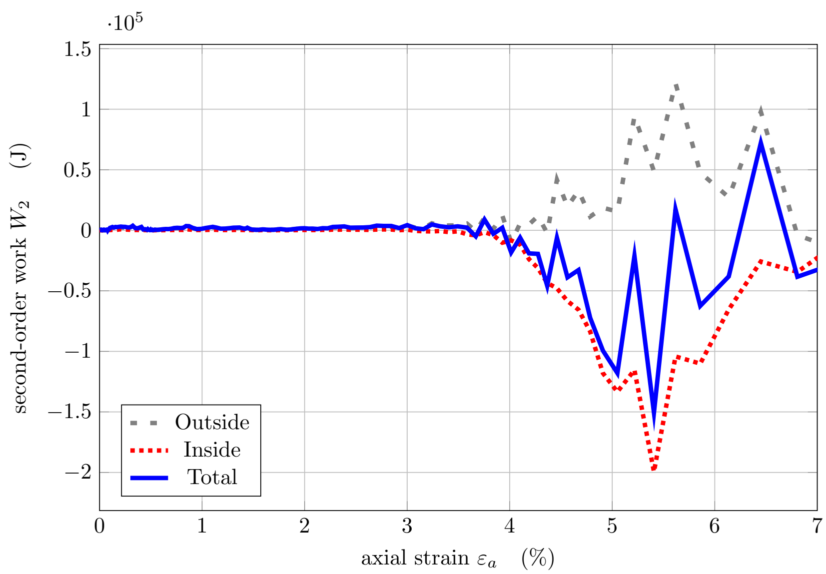

(b) Evolution of the second-order work W_2 (J) against the overall axial strain ε_a (%): inside shear band, outside shear band and total area.

Figure 23: Evolution of the volumetric strain ε_v (%) and the second-order work W_2 (J) with respect to the overall axial strain ε_a (%) for test T1.

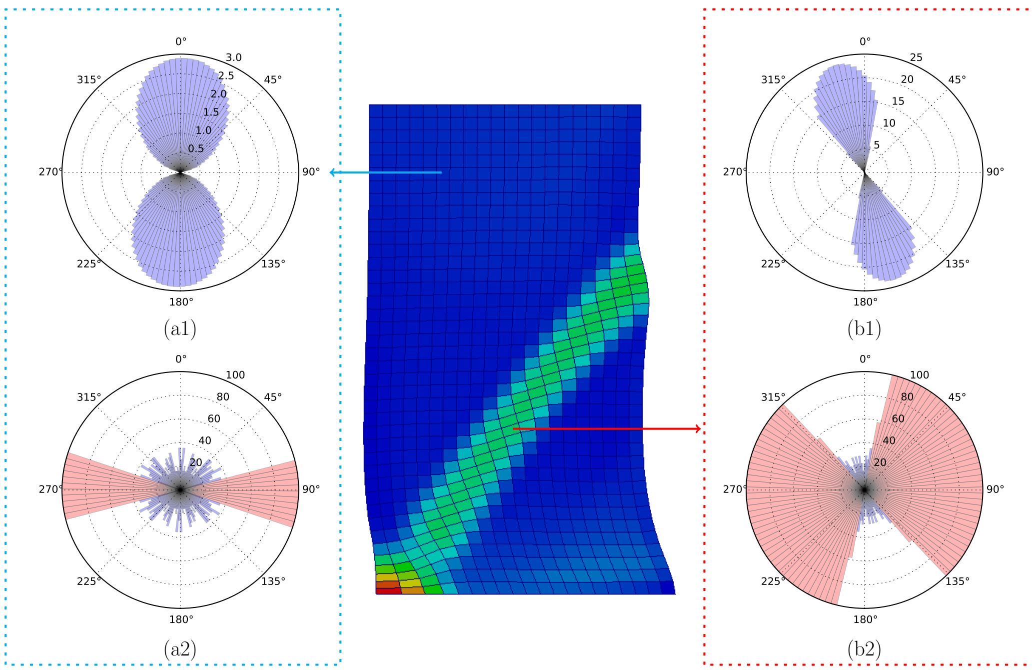

Figure 24: Microscopic variable distributions for Gauss points with inside and outside shear band: (a1) and (b1) integrated microstress $\tilde{\sigma}_n^I(\varphi)$; (a2) and (b2) plastic (blue) and failure (red) percentage of meso-structure along oriented along different directions.

$\tilde{\sigma}_n^I(\varphi) = \iint \omega \tilde{\sigma}_n d\theta d\psi$. By comparing sub-figures in Figure 24, the first remark is that all the micro variables show symmetrical distributions, with symmetry axes oriented along different directions. It is because a significantly shear deformation can be observed inside the shear band. It should be noted that the microstress $\tilde{\sigma}_n^I(\varphi)$ distribution can reflect the force fabric from another side. Similarly, the plastic and failure meso-structure distributions correspond to the contact fabric. From a microscopic point of view, the 3D-H model shows properly anisotropy distributions of both fabric for Gauss points located inside and outside the shear band, but without involving any anisotropy parameter. For the sake of illustration, it can be observed that the magnitude of $\tilde{\sigma}_n^I(\varphi)$ in Figure 24(b1) is much higher than that is in Figure 24(a1), but Figure 24(b1) shows a narrow range. It is because a wide range of failure exists in Figure 24(b2) due to the dilatant behavior inside the shear band. This failure mechanism naturally leads to the anisotropic distribution.

5. Conclusions

A 3D multi-scale approach has been developed and further analysis has been carried out to investigate the occurrence of strain localization along drained triaxial loading paths. To avoid too much sophisticated equations requiring a large number of parameters as introduced in most of conventional phenomenological models, a micromechanically-based model, named 3D-H model, was implemented within a FEM code. The proposed multiscale approach offers a straightforward way to establish the macro-micro relationship wherein the FEM is used to solve BVPs and the 3D-H model is employed as the constitutive relation taking place at Gauss points.

Taking advantage of a micromechanically-based approach, only four parameters are involved. The model parameters were firstly calibrated from comparisons with the experimental data on Ticino sand. Then, drained triaxial tests in plane strain conditions were carried out. A series of aspects were considered, including boundary conditions, material imperfections, initial void ratio and confining stress. A system of shear bands has naturally emerged from a homogeneous specimen, corresponding to a proper bifurcation in the mechanical response of the specimen.

By comparing the deviatoric strain field and the second-order work field, it was found that the sign of second-order work can be considered as an indicator of material instability. After the shear band area is determined, the the material response inside and outside the shear band was separately analyzed. Two Gauss point located inside and outside shear band area were selected and microscopic variable distributions for the two Gauss points were analyzed.

Further researches will be focused on full 3D simulations, involving geotechnical issues.

Acknowledgment

The authors would like to express their sincere thanks to the scholarship from China Scholarship Council (CSC) under the Grant CSC Number 201406250016, the National Natural Science Foundation of China (Grant no. 51579179), the Region Pays de la Loire of France (project RI-ADAPTCLIM) and the French Research Network GeoMech (Multi-Physics and Multi-scale

Couplings in Geo-environmental Mechanics, GDRI CNRS, 2016-2019).

References

[1] Alshibli, K. A., Batiste, S. N., Sture, S., 2003. Strain localization in sand: plane strain versus triaxial compression. Journal of Geotechnical and Geoenvironmental Engineering 129 (6), 483–494.

[2] Andrade, J. E., Avila, C. F., Hall, S. A., Lenoir, N., Viggiani, G., 2011. Multiscale modeling and characterization of granular matter: from grain kinematics to continuum mechanics. Journal of the Mechanics and Physics of Solids 59 (2), 237–250.

[3] Andrade, J. E., Tu, X. X., 2009. Multiscale framework for behavior prediction in granular media. Mechanics of Materials 41 (6), 652–669.

[4] Cambou, B., Dubujet, P., Emeriault, F., Sidoroff, F., 1995. Homogenization for granular materials. European journal of mechanics. A. Solids 14 (2), 255–276.

[5] Chang, C., Yin, Z.-Y., Hicher, P.-Y., 2010. Micromechanical analysis for interparticle and assembly instability of sand. Journal of Engineering Mechanics 137 (3), 155–168.

[6] Chang, C. S., Yin, Z.-Y., 2009. Micromechanical modeling for inherent anisotropy in granular materials. Journal of engineering mechanics 136 (7), 830–839.

[7] Christoffersen, J., Mehrabadi, M. M., Nemat-Nasser, S., 1981. A micromechanical description of granular material behavior. Journal of Applied Mechanics 48 (2), 339–344.

[8] Cundall, P. A., Strack, O. D. L., 1979. A discrete numerical model for granular assemblies. Géotechnique 29 (1), 47–65.

[9] Daouadji, A., Darve, F., Al Gali, H., Hicher, P., Laouafa, F., Lignon, S., Nicot, F., Nova, R., Pinheiro, M., Prunier, F., et al., 2011. Diffuse failure in geomaterials: experiments, theory and modelling. International Journal for Numerical and Analytical Methods in Geomechanics 35 (16), 1731–1773.

[10] Darve, F., Servant, G., Laouafa, F., Khoa, H., 2004. Failure in geomaterials: continuous and discrete analyses. Computer methods in applied mechanics and engineering 193 (27), 3057–3085.

[11] De Saxcé, G., Fortin, J., Millet, O., 2004. About the numerical simulation of the dynamics of granular media and the definition of the mean stress tensor. Mechanics of Materials 36 (12), 1175–1184.

[12] Desrues, J., Chambon, R., Mokni, M., Mazerolle, F., 1996. Void ratio evolution inside shear bands in triaxial sand specimens studied by computed tomography. Géotechnique 46 (3), 529–546.

[13] Desrues, J., Viggiani, G., 2004. Strain localization in sand: an overview of the experimental results obtained in grenoble using stereophotogrammetry. International Journal for Numerical and Analytical Methods in Geomechanics 28 (4), 279–321.

[14] Guo, N., Zhao, J. D., 2013. A hierarchical model for cross-scale simulation of granular media. In: AIP conference proceedings. Vol. 1542. pp. 1222–1225.

[15] Guo, N., Zhao, J. D., 2014. A coupled fem/dem approach for hierarchical multiscale modelling of granular media. International Journal for Numerical Methods in Engineering 99 (11), 789–818.

[16] Guo, N., Zhao, J. D., 2016. 3d multiscale modeling of strain localization in granular media. Computers and Geotechnics.

[17] Guo, N., Zhao, J. D., 2016. Parallel hierarchical multiscale modelling of hydro-mechanical problems for saturated granular soils. Computer Methods in Applied Mechanics and Engineering 305, 37–61.

[18] Hadda, N., Nicot, F., Bourrier, F., Sibille, L., Radjai, F., Darve, F., 2013. Micromechanical analysis of second order work in granular media. Granular matter 15 (2), 221–235.

[19] Han, C., Drescher, A., 1993. Shear bands in biaxial tests on dry coarse sand. Soils and Foundations 33 (1), 118–132.

[20] Hibbitt, Karlsson, Sorensen, 2001. ABAQUS/Explicit: User's Manual. Vol. 1. Hibbitt, Karlsson and Sorenson Incorporated.

[21] Liu, Y., Sun, W., Yuan, Z., Fish, J., 2016. A nonlocal multiscale discretecontinuum model for predicting mechanical behavior of granular materials. International Journal for Numerical Methods in Engineering 106 (2), 129–160.

[22] Love, A. E. H., 2013. A treatise on the mathematical theory of elasticity. Vol. 1. Cambridge University Press.

[23] Mehrabadi, M. M., Nemat-Nasser, S., Oda, M., 1982. On statistical description of stress and fabric in granular materials. International Journal for Numerical and Analytical Methods in Geomechanics 6 (1), 95–108.

[24] Meier, H. A., Steinmann, P., Kuhl, E., 2008. Towards multiscale computation of confined granular media–contact forces, stresses and tangent operators. Technische Mechanik 28 (1), 32–42.

[25] Meier, H. A., Steinmann, P., Kuhl, E., 2009. On the multiscale computation of confined granular media. In: ECCOMAS Multidisciplinary Jubilee Symposium. Springer, pp. 121–133.

[26] Nguyen, H. N., Prunier, F., Djeran-Maigre, I., Nicot, F., 2016. Kinetic energy and collapse of granular materials. Granular Matter 18 (1), 1–10.

[27] Nicot, F., 2003. Constitutive modelling of a snow cover with a change in scale. European Journal of Mechanics-A/Solids 22 (3), 325–340.

[28] Nicot, F., Darve, F., 2011. The H-microdirectional model: accounting for a mesoscopic scale. Mechanics of Materials 43 (12), 918–929.

[29] Nicot, F., Darve, F., Dat Vu Khoa, H., 2007. Bifurcation and second-order work in geomaterials. International journal for numerical and analytical methods in geomechanics 31 (8), 1007–1032.

[30] Nicot, F., Darve, F., Group, R., 2005. A multi-scale approach to granular materials. Mechanics of materials 37 (9), 980–1006.

[31] Nicot, F., Sibille, L., Donze, F., Darve, F., 2007. From microscopic to macroscopic second-order work in granular assemblies. Mechanics of materials 39 (7), 664–684.

[32] Nicot, F., Xiong, H., Wautier, A., Lerbet, J., Darve, F., 2017. Force chain collapse as grain column buckling in granular materials. Granular Matter 19 (2), 18.

[33] Prunier, F., Laouafa, F., Lignon, S., Darve, F., 2009. Bifurcation modeling in geomaterials: From the second-order work criterion to spectral analyses. International Journal for Numerical and Analytical Methods in Geomechanics 33 (9), 1169–1202.

[34] Prunier, F., Nicot, F., Darve, F., Laouafa, F., Lignon, S., 2009. Three-dimensional multiscale bifurcation analysis of granular media. Journal of Engineering Mechanics 135 (6), 493–509.

[35] Radjaï, F., Dubois, F., 2011. Discrete-element modeling of granular materials. Wiley-Iste.

[36] Rechenmacher, A. L., 2006. Grain-scale processes governing shear band initiation and evolution in sands. Journal of the Mechanics and Physics of Solids 54 (1), 22–45.

[37] Rudnicki, J. W., Rice, J., 1975. Conditions for the localization of deformation in pressure-sensitive dilatant materials. Journal of the Mechanics and Physics of Solids 23 (6), 371–394.

[38] Sibille, L., Nicot, F., Donze, F. V., Darve, F., 2007. Material instability

in granular assemblies from fundamentally different models. International Journal For Numerical and Analytical Methods in Geomechanics 31 (3), 457–481.

[39] Vardoulakis, I., Goldscheider, M., Gudehus, G., 1978. Formation of shear bands in sand bodies as a bifurcation problem. International Journal for numerical and analytical methods in Geomechanics 2 (2), 99–128.

[40] Voigt, W., 1889. Ueber die beziehung zwischen den beiden elasticitätsconstanten isotroper körper. Annalen der Physik 274 (12), 573–587.

[41] Wan, R., Nicot, F., Darve, F., 2017. Failure in Geomaterials: A Contemporary Treatise. Elsevier.

[42] Wan, R., Pinheiro, M., Daouadji, A., Jrad, M., Darve, F., 2013. Diffuse instabilities with transition to localization in loose granular materials. International Journal for Numerical and Analytical Methods in Geomechanics 37 (10), 1292–1311.

[43] Wang, K., Sun, W., 2016. A semi-implicit discrete-continuum coupling method for porous media based on the effective stress principle at finite strain. Computer Methods in Applied Mechanics and Engineering 304, 546–583.

[44] Wang, K., Sun, W., Salager, S., Na, S., Khaddour, G., 2016. Identifying material parameters for a micro-polar plasticity model via x-ray micro-ct images: lessons learned from the curve-fitting exercises. International Journal for Multiscale Computational Engineering 14 (4), 389–413.

[45] Xiong, H., Nicot, F., Yin, Z., 2017. A three-dimensional micromechanically based model. International Journal for Numerical and Analytical Methods in Geomechanics.

[46] Yin, Z.-Y., Chang, C. S., Hicher, P.-Y., 2010. Micromechanical modelling for effect of inherent anisotropy on cyclic behaviour of sand. International Journal of Solids and Structures 47 (14), 1933–1951.

[47] Yin, Z.-Y., Chang, C. S., Hicher, P.-Y., Karstunen, M., 2009. Micromechanical analysis of kinematic hardening in natural clay. International Journal of Plasticity 25 (8), 1413–1435.

[48] Yin, Z.-Y., Hattab, M., Hicher, P.-Y., 2011. Multiscale modeling of a sensitive marine clay. International Journal for Numerical and Analytical Methods in Geomechanics 35 (15), 1682–1702.

[49] Yin, Z.-Y., Zhao, J., Hicher, P.-Y., 2014. A micromechanics-based model for sand-silt mixtures. International journal of solids and structures 51 (6), 1350–1363.

[50] Zhu, H., Nguyen, H. N., Nicot, F., Darve, F., 2016. On a common critical state in localized and diffuse failure modes. Journal of the Mechanics and Physics of Solids 95, 112–131.